Selection of domains for coarse and fine levels of description in mixed-potential simulations

P.A. DEYMIER[a,*], KIDONG OH[a], KRISHNA MURALIDHARAN[b],
G. FRANTZIKONIS[c] and K. RUNGE[b]

[a]*Department of Materials Science and Engineering, The University of Arizona, Tucson AZ 85721, USA*
[b]*Quantum Theory Project, Departments of Physics and of Chemistry, University of Florida, Gainesville FL 32611, USA*
[c]*Department of Civil Engineering and Engineering Mechanics, The University of Arizona, Tucson, AZ 85721, USA*

Abstract. An example of a mixed-potential molecular dynamics simulation is presented for amorphous silica. Pair potentials are used in the roles of embedding and embedded regions to allow us to study on-the-fly selection of a region for the more accurate description by embedded potentials. Brittle fracture with fast crack growth is the example that we choose to elucidate the characteristics of an amorphous system that lead to reliable prediction of the location of the initial fracture in the unbiased system. We conclude that a properly chosen wavelet analysis will permit such on-the-fly identification of those regions in a multi-scale simulation whose properties need to be described at the highest available accuracy.

Keywords: brittle fracture, glass, modeling, molecular dynamics, multiscale, wavelet

1. Introduction

In the present study, we identify and address several issues associated with atomistic simulations of brittle fracture in amorphous glass involving quantum mechanical (QM) models combined with classical atomistic models. We identify these multi-scale simulations as mixed-potential simulations. Mixed-potential simulations belong to the family of concurrent multi-scale methods in the sense that different regions of the same material are represented with different level of accuracy by different atomic-interaction models. Mixed-potential simulations are not limited to QM methods in atomistic level calculation. Rather, they may involve the simple use of two classical inter-atomic potentials (representing bonds with different level of complexity) applied at different locations within a heterogeneous model system such that a more accurate but computationally complex potential is imposed on regions where bond rearrangement or large bond stretching occurs while a coarser more approximate potential function is employed in regions of low strain. This approach would entail proper identification of the location and spatial extent of regions that are to be treated with the different potentials, in order to capture the mechanisms of failure. In the case of materials with cracks (or flaws), the identification of different regions is trivial and

---
*To whom correspondence should be addressed, E-mail: deymier@email.arizona.edu

one only needs to use the more accurate potential to model the crack-tip. In contrast, however, identification of different regions is not straight-forward in modeling the brittle fracture of initially flaw-free materials. Methods need to be devised to identify regions of high stress (where failure could occur) and model them by the more accurate potential much before failure occurs. In addition, flaw-free materials could fail via spalling, a process in which there could be more than one region of failure. This possibility poses problems as then one needs to address the dynamics of the location/relocation of the different regions without perturbing the dynamical behavior of failure. Another crucial aspect of mixed-potentials is the extent of mismatch between the potential functions with respect to bond behavior and its impact on the dynamics of failure.

In this article, we consider a simple mixed-potential model of amorphous silica – a model brittle material – incorporating a "high-accuracy" inter-atomic potential (embedded potential) with an approximate one (embedding potential). This model enables us to quantify and unravel the criteria and constraints that mixed-potential, multi-scale simulations methods need to satisfy in order to mimic seamlessly the failure behavior of a large scale high-accuracy system. The efficacy of methods capable of locating failure regions in flaw-free amorphous silica samples is discussed in this work.

2. Models and methods

We focus on the brittle fracture of amorphous silica; a-SiO_2. This structure is generally recognized to be an open network of corner-sharing tetrahedra linked by bridging oxygens. Wiederhorn [1, 2] has described a three regime behavior for the brittle fracture of a-SiO_2 wherein regimes 1 and 2 are limited by environmental effects (slow crack growth). We will concern ourselves with Wiederhorn's regime 3, in which environmental effects can be neglected and the high crack growth velocities are limited by the mechanical properties of the material (sudden fracture). It is pertinent in this context to note that the strength of ultra-pure silica fibers was measured as $18.0\,GPa$ by Proctor [3], a value about two orders of magnitude higher than the measured strength of bulk silica.

We use molecular dynamics (MD) to study the sudden failure of a-SiO_2 with a mixed-potential simulation. (Proper treatment of potentials for silica is considered in the third and fourth articles of this section.) Here we select the first inter-atomic potential (embedded potential mimicking the "high accuracy" potential) to be a modified version of the BKS potential [4]. That potential is based on cluster model calculations refined by comparison with bulk experimental properties. It diverges at very short inter-atomic distance. To avoid the divergence, we use a modified BKS form proposed by Corrales [4] that incorporates an 24–6 Lennard–Jones potential function. This modified BKS pair potential takes the form

$$\phi_{ij} = \frac{q_i q_j}{r_{ij}} + A_{ij} e^{-B_{ij} r_{ij}} - \frac{C_{ij}}{r_{ij}^6} + 4\varepsilon_{ij} \left(\frac{\sigma_{ij}}{r_{ij}}\right)^{24} - 4\varepsilon_{ij} \left(\frac{\sigma_{ij}}{r_{ij}}\right)^6 \tag{1}$$

where r_{ij} is the distance between atom i and j, and q_i is a charge of atom i. The effective Si and O atomic charges are $2.4e$ and $-1.2e$ (e is the electron charge magnitude), respectively, and the other parameters are listed in Table 1.

Table 1. Parameters of the modified BKS potential

Atom pairs	A_{ij} (eV)	B_{ij} (Å^{-1})	C_{ij} (eV/ Å^6)	$\varepsilon_{ij}(eV)$	σ_{ij}(Å)
Si–O	18003.7572	4.87318	133.5381	1.12245×10^{-2}	1.3100
O–O	1388.7730	2.76000	175.0000	3.5653×10^{-4}	2.2000
Si–Si	–	–	–	12.6387	0.4200

The second potential (representing here a less accurate potential or an embedding potential) is based on the charge transfer (CT) potential that was suggested by Alavi et al. [5]. Its functional form is the same as that of the modified BKS potential, but the charges on a pair of atoms are evaluated by the following:

$$q_i = q_i^a - \Delta q \sum_j \tfrac{1}{2} \left[1 - \tanh\left(\tfrac{r_{ij} - R_{ab}}{\xi} \right) \right],$$
$$q_j = q_j^b - \Delta q \sum_i \tfrac{1}{2} \left[1 - \tanh\left(\tfrac{r_{ij} - R_{ab}}{\xi} \right) \right] \tag{2}$$

where $q_{Si} = 4.0e$, $q_O = -2.0e$, $\Delta q = 0.4523$, $R_{ab} = 1.90$ Å, and $\xi = 0.29$ Å.

Because these charges are functions of r_{ij}, their derivatives with respect to interatomic distance should be calculated as part of the force on an each atom. However, we neglect that contribution to the forces, since the derivative correction amounts to less than 0.5% of the exact force calculation and is computationally expensive.

In the limit of very small bond expansions, the CT potential converges toward the modified BKS potential. It is therefore expected that the elastic moduli of a modified BKS glass and of a CT glass converge to the same value in the limit of small strains. It is also important to note that the CT potential leads to stronger bonds than the modified BKS potential for large deformations. As will be seen later, the strength of a homogeneous SiO_2 glass simulated with a BKS potential is lower than that of the same system modeled with the CT potential. This relationship reflects the general requirement for concurrent multi-scale simulation: the stronger potential (here the CT potential) must be the embedding potential and the weaker potential (modified BKS potential) must be the embedded potential. This constraint will bias the strength of the mixed-potential system toward that of the weaker region (i.e. the desired embedded high-accuracy region), thereby providing a rational basis for expecting the mixed-potential model to approach the behavior of a larger system treated solely with high-accuracy interactions.

As a first step, we use the modified BKS potential exclusively to simulate silica glasses and study their response to external uniaxial strain applied uniformly throughout the material. All MD simulations reported here were conducted at constant temperature ($T = 300$ K) using a Nose–Hoover thermostat [6]. Surface effects that may arise from the simulation of a small number of atoms are reduced by imposition of periodic boundary conditions (PBC) to the simulation cell in all spatial directions. The size of the MD time integration step was one femtosecond and the equations of motion of the atoms were solved with the Verlet–Beeman integrator [7]. The long-range Coulomb interactions are treated with the Ewald summation method [8].

Table 2. Total number of atoms and dimensions (Cartesian edge lengths for the simulation box) of equilibrated, zero-pressure glass samples. The samples were quenched step-wise with a temperature decrement ΔT and an equilibration time between decrements of Δt

Sample	N	L_x(Å)	L_y(Å)	L_z(Å)	ΔT (K)	Δt (ps)
1	8640	99.96	29.99	41.85	1000	8.0
2	8640	99.96	29.99	41.85	992	8.0
3	8400	99.30	34.74	34.68	992	8.0

To improve the statistics on the failure behavior of a-SiO_2 glass, we prepared three different samples (samples 1, 2, and 3). Typically in MD simulations, silica glass is prepared by quenching β-cristobalite (because of the similar densities). In our case, the first two samples consist of 8640 atoms (2880 Si and 5760 O atoms), while the third sample contains 8400 atoms. All initial configurations were heated to 8000 K and step-wise quenched to 300 K as prescribed by Huff et al. [9]. The resultant densities of the samples were identical, 2.28 g/cm^3, close to the experimental value. Since the structures of the quenched glasses are very sensitive to initial conditions and cooling rates, we quenched the three samples with different initial velocities and slightly different cooling rates as shown in Table 2, which also contains information about the geometry of the samples. Obviously, an advantage of preparing glasses with different local structures is that we could compare and contrast their fracture dynamics, which in turn would be a valuable learning tool to help us identify domains that are more susceptible to failure.

All the glass samples were mechanically tested by imposing uniform uniaxial strain rates ranging from 0.1/ps to 0.002/ps. As expected, the stress response (calculated via the virial theorem) was similar for the three glass samples at all strain rates (though the location of failure was different for the three samples), and the strength of each glass increased with increasing strain rate. As an example, the stress–strain curves for sample 1 at different strain rates are displayed in Figure 1, with labels specifying the extent of three primary regions; see the third article in this section for a more detailed discussion.

In addition, a comparison of the stress responses for all three samples (strain rate = 0.01/ps) and their locations of failure is given in Figure 2. The variability in strength and failure strain indicates that heterogeneities within the structure of the glass play an important role in failure behavior. This observation is particularly evident regarding the variability in the failure location of the three samples. In order to identify the location(s) of failure, or equivalently, the 'weak' regions in a material, we looked for distinct signatures that characterized such regions. K. Muralidharan et al. (submitted) have examined atomic-level fracture mechanisms of silica glass in detail. They correlated the growth of nano-scale and sub-nano-scale voids to the fracture process and showed that these voids serve as nucleation regions for localized structural transformations. Specifically, past the elastic limit, these voids are characterized by the presence of highly strained edge-sharing two membered (2-M) silica rings in their vicinities, as opposed to the corner-sharing structure of the bulk. The structural
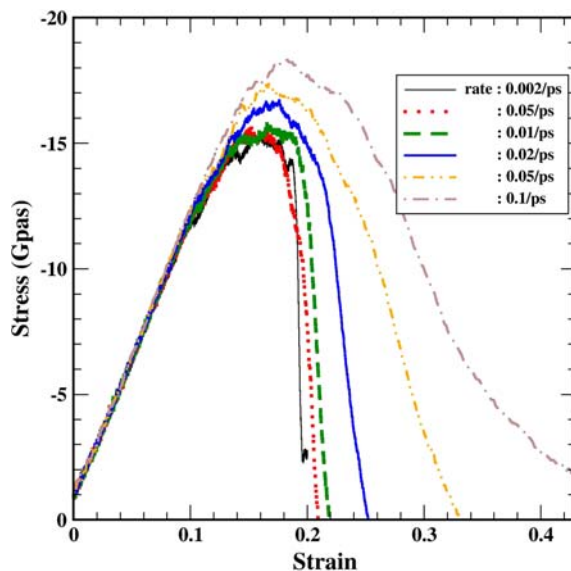
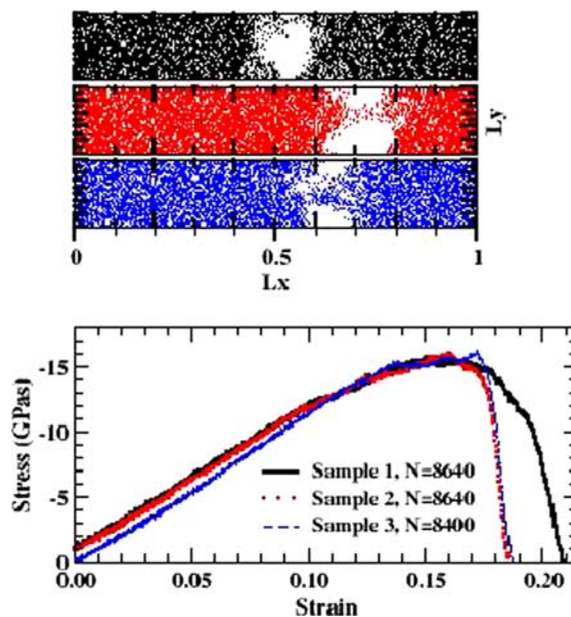*Figure 1.* Stress–strain curve for sample 1 for different strain rates.

Figure 2. Stress versus strain curves with the modified BKS potential for the three glass samples studied at a strain rate = 0.01/ps along the X-direction. Samples 1, 2 and 3 fail at approximately 0.52, 0.7 and $0.65L_x$, where L_x is the length of the simulation box in the X-direction.

transformations that occur near these voids are rapid and involve the initial formation of singly coordinated oxygen and tri-coordinated silicon atoms. Based on the foregoing observations, one could infer that regions in a material that are more susceptible to failure could be characterized in terms of local atomic densities (a proxy for the voids), coordination of atoms, and presence of 2-M rings.

Since failure of the modified-BKS model glasses at constant strain rate involves characterization of defects, density, and local stress on scales ranging from the atomic to those associated with nano-voids or coalescing voids, any diagnostic tool for predicting regions of failure must be sensitive over such a large range of lengths. For this reason, we use wavelet analysis to characterize the evolution of the glass spatial structure during straining and failure. In particular, by analogy with its use in signal and image processing, we have used wavelet transforms to analyze MD outputs [10]. A wavelet transform can be conceptualized as a sort of "mathematical microscope" that provides ready information on the intricate structure of a "pattern." The wavelet coefficients provide local information on the nature of any function at various scales (ranging from the very fine to the coarsest), hence one can identify the important and often, dominant, scale(s) by examining the coefficients at every scale. The wavelet transform thus constitutes an ideal tool for multi-scale modeling.

In one-dimension, a wavelet $\psi(x)$ transforms a fluctuating function $f(x)$ [11]:

$$W_f(a,b) = \int_{-\infty}^{\infty} f(x)\,\psi_{a,b}(x)\,dx \tag{3}$$

The two-parameter family of functions, $\psi_{a,b}(x) = \left(1/\sqrt{a}\right)\psi\left(\frac{xb}{a}\right)$ is obtained from a single one, ψ, called the mother wavelet, through dilations by the scaling factor a and translations by the factor b. The factor $1/\sqrt{a}$ is included for normalization. The parameter a can take any positive real value, and the fluctuations of $f(x)$ at position b are measured at the scale a. Given the wavelet coefficients $W_f(a,b)$ associated with a function f, it is possible to reconstruct f at a range of scales between s_1 and s_2 ($s_1 \leqslant s_2$) through the inversion formula

$$f_{s_1,s_2}(x) = \frac{1}{c_\psi} \int_{s_1}^{s_2} \int_{-\infty}^{\infty} W_f(a,b)\,\psi_{a,b}(x)\,db\,\frac{da}{a^2} \tag{4}$$

Setting $s_1 \to 0$ and $s_2 \to \infty$ reconstructs the original function over all scales. When discretized, wavelet analysis can be performed with fast algorithms. In the present study we employ the discrete Haar's wavelet [12]. whence Eq. (4) becomes:

$$f_M(x) = \sum_{m=-\infty}^{-1} \psi_{m0}(x)C_{m0}(x) + \sum_{m=0}^{M}\sum_{n=0}^{2^M} \psi_{mn}(x)C_{mn}(x) \tag{5}$$

Here M is the expansion order and $f_M(x)$ is the Mth order approximation for the original fluctuating signal function, $f(x)$. The wavelet coefficients are defined through Eq. (3): $C_{mn}(x) = \int f(x)\psi_{mn}(x)dx$, with the Haar's wavelet basis set given by

$$\begin{aligned}
\psi_{mn}(x) &= \sqrt{2^m} && \text{if } 0 \leqslant 2^m x - n < {}^1\!/_2 \\
&= -\sqrt{2^m} && \text{if } {}^1\!/_2 \leqslant 2^m x - n < 1. \\
&= 0 && \text{otherwise}
\end{aligned} \tag{6}$$

Figure 3 illustrates the Haar's wavelet Mth order approximations of some arbitrary function, $f(x)$, discretized over 64 points between 0 and 1. As the order, M, decreases, the approximations become coarser.

Wavelet-based methods have been used to bridge the spatial scales of atomistic computational methodologies to those of coarse grain simulation techniques [13] as
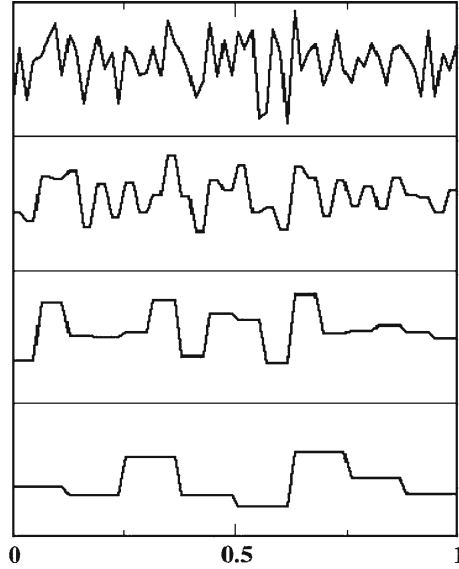
Figure 3. Representations of a function, $f(x)$, with the Haar's wavelet transformations. From the top, original signal ($M=5$), $M=4$, $M=3$, and $M=2$, where M is the expansion order of the transformation.
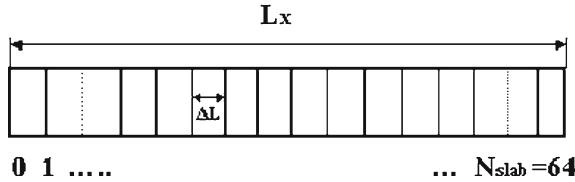

Figure 4. Division of the MD simulation cell into 2^6 subcells (slabs) along the direction X of elongation of the glass samples. The width of a slab $\Delta L = L_x/64$.

well as to bridge time scales between discrete and continuum models [14]. In the present article, we use wavelet approximations to filter one-dimensional maps of local atomic density, of the number of singly coordinated oxygen atoms, and as well, of the stress along the direction of elongation of the glass samples. The simulated system is divided into 64 slabs as illustrated in Figure 4.

The inhomogeneity in atomic density along the glass sample was quantified simply by counting the number of atoms in each slab, $n(I)$, $I = 1, N_{slab}$. We also identified and counted the number of singly coordinated oxygen atoms in each slab, $n_{O1}(I)$, as a measure of the inhomogeneity in defect concentration. Finally, one-dimensional variations in stress are also studied.

We calculated the local stress at a slab, i, by applying the virial theorem to each slab. Thus the local stress tensor, σ_{mn}, is given by

$$\sigma_{mn} = \frac{1}{3\Omega} \left(\sum_{i=1}^{N} m_i v_{i,m} v_{i,n} + \sum_{i=1}^{N} \sum_{j>i}^{N} r_{ij,m} F_{ij,n} \right) \tag{7}$$
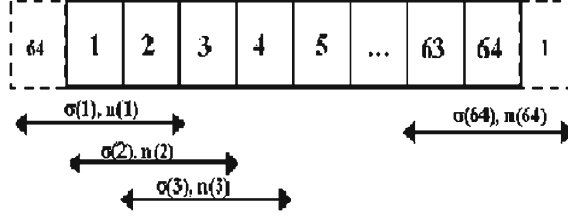
Figure 5. Scheme used to calculate a one-dimensional map of local stress along the strained glass sample.

where m and n represent Cartesian directions, Ω is the volume in which the stress is evaluated, N is the number of atoms in Ω, F_{ij} is the inter-atomic force between atoms i and j separated by r_{ij} in cells $I-1$, I and $I+1$, with $I=1$, N_{slab}, m_i and v_i are the mass and velocity of atom i. For instance, to calculate the local stress in slab 2, $\sigma(2)$ if we suppress subscripts, in Figure 5, we use Eq. (7) but restricted such that both atoms i and j must be in slab 1, 2, or 3. The corresponding volume is $3\Omega/64$. Since the atomic density may vary significantly from slab to slab, we define a local stress per particle, $\sigma(I)/n(I)$. We also calculated the local stress at some slab I as a function of the number of adjacent slabs used in the virial equation, that is, $\sigma^{Q+1}(I)$ where Q is the number of neighboring slabs. In Figure 5, we illustrate the calculation of the local stress, $\sigma^3(I)$ using the slab of interest and its two nearest neighbors. In the case of an even value of $Q+1$, the slabs used for the calculation of the local stress at I are arranged asymmetrically with respect to the slab of interest I.

3. Results

3.1. "On-the-fly" identification of the failure domain

One of the major goals of multi-scale simulation of failure of brittle materials is to identify how to partition the simulated system in order to apply models of the system at different scales *as the simulation is underway.* Though self-evidently an important task, such "on-the-fly" domain identification is relatively little developed. In this section, we test and analyze the wavelet-based approach described in Section 2 as a potential automated identifier of the partitions needed for the application of mixed-potential multi-scale simulations. For that purpose we investigate the time evolution of the spatial evolution of three quantities: the atomic density, the number of singly coordinated oxygen atoms, and the local stress per particle. We focus this investigation on the modified-BKS glass. All the results reported are for a strain rate of 0.005/ps along the X-direction. The stress versus strain curve for that sample glass at that strain rate was given in Figure 1.

Figure 6 reports the variation with strain of the second-order wavelet approximation, $n_{M=2}(x)$ of the atomic density, $n(x)$. Beyond the elastic regime (region I in Figure 1), the location of the slab with the lowest atomic density undergoes large fluctuations for strains in the interval [0.1–0.15]. This interval corresponds to the region of the stress–strain curve where the glass has reached its maximum strength and void formation and coalescence occurs (region II in Figure 1). Beyond that region (strain > 0.17, i.e. in region III of Figure 1) the location with lowest atomic
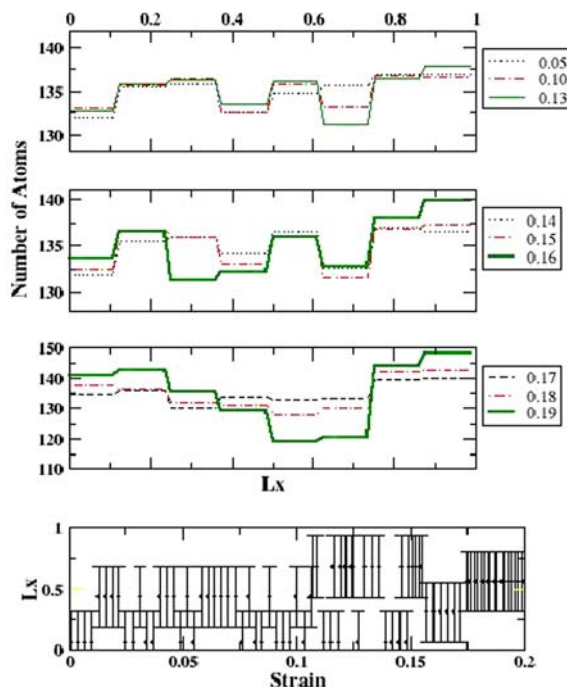
Figure 6. The upper three panels show the changes in the second-order wavelet approximation for the distribution of atomic density along the strained glass sample 1 at several values of strain. The bottom panel illustrates the location of the slab with the lowest atomic density as a function of strain. The error bars are guides to the eye delimiting a region of width $0.52L_x$ centered upon the slab with lowest density.

density converges to $0.52L_x$ that corresponds to the final position of failure of the glass sample. The level of convergence depends on the order of the wavelet approximation to the local density function. Indeed Figure 7 shows the evolution of the location of the slab with the lowest atomic density as a function of strain for three different expansion orders. The convergence toward the location of failure in region III of the stress–strain curve becomes poorer as the order of the wavelet expansion increases, that is, as the wavelet approximation approaches the original function. On the other hand, in regions I and II, the lowest-order approximation ($M = 2$) exhibits larger fluctuations than its higher-order counterparts ($M = 3$ and 4) an indication that the glass must contain a small-scale, low-density defect in the slab located at $\sim 0.8L$ that the lowest order approximations to the atomic density is able to filter out.

Wavelet approximations to the atomic density appear to be sensitive to the details of the initial configuration as well as to the scale of defects (e.g. nano-scale voids) that may form as a result of straining. This aspect is illustrated in Figure 8, which shows the evolutions of the location of the slab with lowest particle density with different wavelet expansion orders for the glass sample 2. Here higher variability is observed for $M = 4$ than for $M = 2$. The order $M = 2$ approximation still appears to give the best level of convergence toward the final location of failure ($\sim 0.7L_x$). Similar results are observed for the other glass samples with variability in the behavior associated with differences in glass structure and stress versus strain responses.
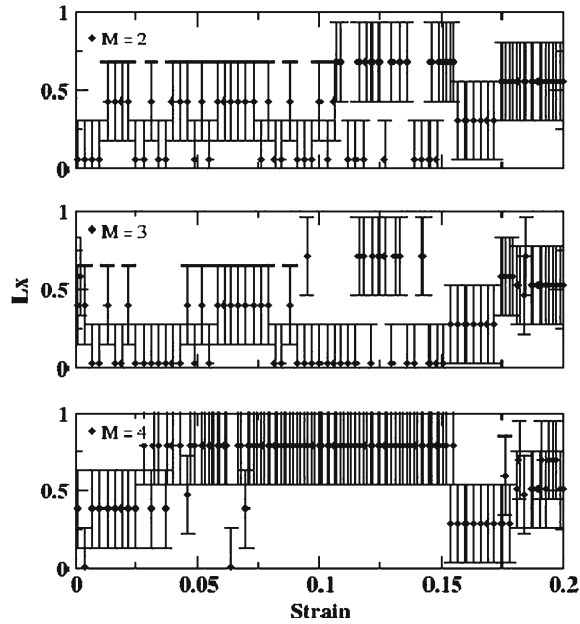
Figure 7. Evolutions of the center of lowest particle density with different wavelet expansion orders, from top to bottom, $M = 2$, 3, and 4 for sample 1.
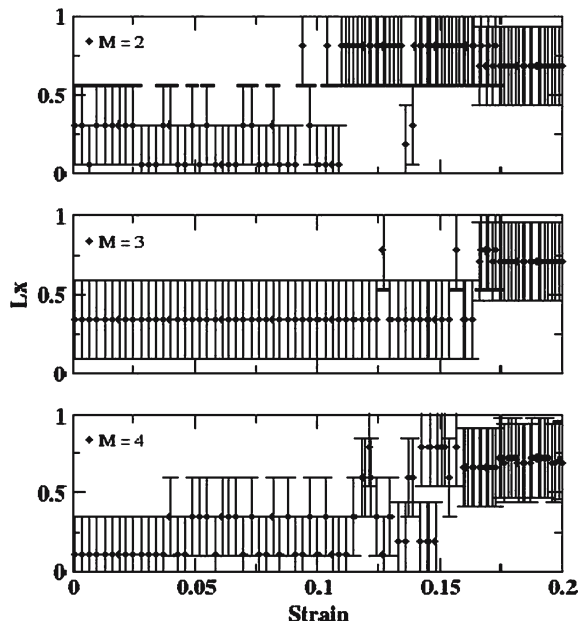

Figure 8. Evolution of the center of lowest particle density with different wavelet expansion orders, from top to bottom, $M = 2$, 3, and 4 for sample 2.

We also calculated the third-order wavelet approximations of the distribution of singly coordinated ("1C") oxygen atoms along the glass sample 1 as a function of strain. Figure 9 shows that initially the glass sample exhibits a non-uniform distribution of 1C-oxygen defects. Large fluctuations in the distribution of defects occur in
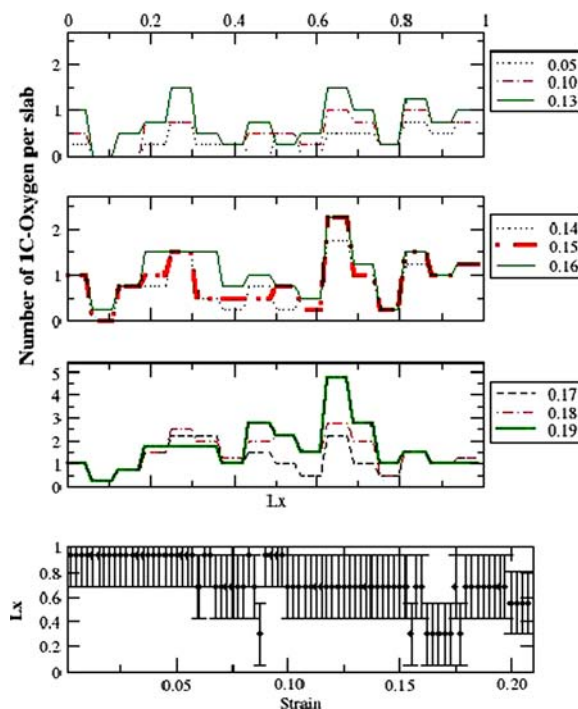
Figure 9. The upper three panels show the changes in the third-order wavelet approximation for the number of singly coordinated oxygen atoms along the strained glass sample 1 at several values of strain. The bottom panel illustrates the location of the slab with the highest number of singly coordinated oxygen atoms as a function of strain. The error bars are guides to the eye delimiting a region of width $0.5L_x$ centered on the slab with highest number of one-coordinated oxygen atoms.

the region II of the stress–strain curve (strain between 0.15 and 0.17). Beyond region II of the stress–strain curve, the defect content increases drastically at the location of failure. The behavior of the distribution of 1C-oxygen atoms parallels that of the local density.

Finally, in Figure 10, we present the variation of the location of the slab with highest tensile stress per particle, calculated from the second-order wavelet approximation for the local stress per particle, as a function of strain in the case of glass sample 1. This evolution is reported for several values of the number of neighboring slabs used to calculate the local stress at slab I, $\sigma^{Q+1}(I)$. Both $Q=1$ and 2 give the results most consistent with the behavior observed in the wavelet approximations to the local atomic density and the local number of singly coordinated oxygen atoms, namely little variation in the location of the highest tensile stress during the elastic deformation of the sample, followed by large fluctuations in the region where nano-voids form and finally convergence to the location of failure in the region III of the stress versus strain curve.

In summary, wavelet expansion to order 2 of the local density, the number of one-coordinated oxygen defects, and the tensile stress per particle appears to provide a useful description in real computational time of the evolution of glass samples subjected to a constant strain rate of 0.005/ps. The wavelet approximations to the actual distributions of density, defects and stress along the sample provide a useful means
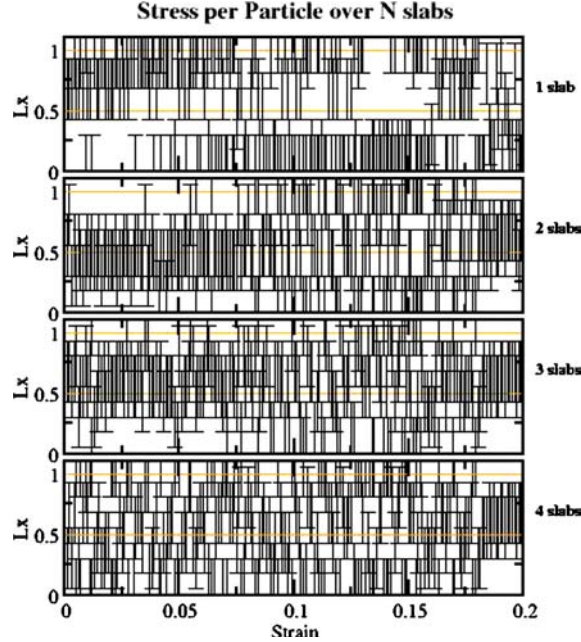
Stress per Particle over N slabs

Figure 10. Location of the slab with the highest tensile stress per particle as a function of strain. From top to bottom the local stress is calculated with different number of slabs, $Q+1=1$, 2, 3, and 4; recall discussion of Eq. (7). The error bars are guides to the eye delimiting a region of width $0.5L_x$ centered on the slab with highest tensile stress. The highest tensile stress per particle is obtained from a wavelet approximation of order 2, $\{\sigma^{Q+1}(I)/n(I)\}_{N=2}$ to the local stress per particle.

of filtering the rapidly varying elements of the distributions. These approximations enable a robust, on-the-fly identification of the incipient failure location at the transition between region II and region III of the stress–strain curve.

3.2. STATIC MIXED-POTENTIAL MULTI-SCALE SIMULATIONS

In this subsection, we turn attention to the behavior of mixed-potential glass samples. The simulation cell is divided into two regions, 1 and 2, in which the inter-atomic forces are calculated from the CT potential (region 1) and the modified-BKS potential (region 2). Since the CT and modified BKS potentials have the same nominal functional form and differ only by the charge on the respective ions, the ionic charges inside region 2 are unchanged while the ionic charges inside region 1 are redistributed according to Eq. (2) between pairs of ions only within that region. Total charge thus is conserved inside regions 1 and 2. The force between two ions, i and j, located on the two sides of the boundary between regions 1 and 2 is calculated straightforwardly from Eq. (1) by using the respective charges of these two ions. Two parameters are used to characterize the geometry of the mixed-potential system, the position of region 2 along the X-direction defined as P the percentage of the system length and the width of the region 2, W (see Figure 11).

The behavior of the mixed-potential system will be analyzed by comparison with two homogeneous reference systems, namely sample 1, in which all interactions are calculated with the BKS potential ($W = L$) and, then again with only the CT
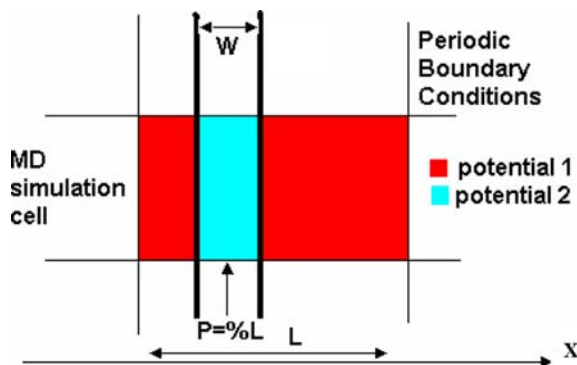
Figure 11. Schematic representation of the static mixed-potential simulation cell. The center location and width of the region 2 where atoms interact via the modified-BKS potential are defined as *P* and *W*, respectively. Atoms interact via the CT potential in region 1. The calculation of inter-atomic forces between atoms across the boundaries bordering regions 1 and 2 is explained in the text. Periodic boundary conditions are applied in all spatial directions.
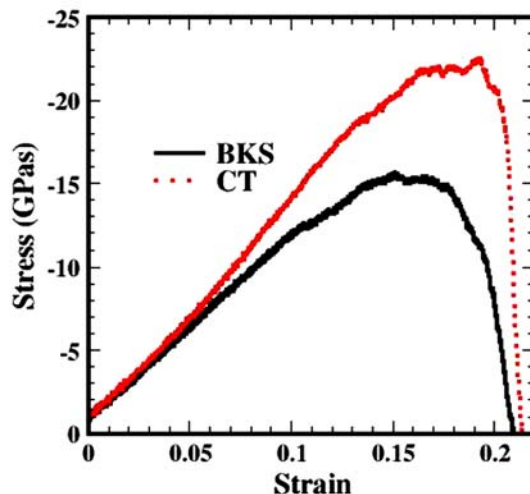

Figure 12. Stress–strain curves obtained by applying a constant strain rate, 0.005/ps to two homogeneous glasses, pure BKS and pure CT (sample 1). The CT and BKS glasses fail at $0.63L_x$ and $0.52L_x$, respectively.

potential ($W = 0$). The stress–strain curves of these two samples under constant strain rate of 0.005/ps are displayed in Figure 12. The two reference systems possess the same elastic modulus at zero strain. Owing to its stronger bonds, the strength of the CT glass significantly exceeds that of the BKS system. In that respect, the CT potential is the embedding potential and the modified BKS potential is the embedded potential. Note that the failure strain of the CT glass is only slightly higher than that of the BKS glass.

To apply a constant strain rate, $\dot{\varepsilon}$, to the simulated glasses, we expand the simulation cell uniformly at regular time intervals. That is, the length of the simulation cell, L_x, evolves in time according to $L_x(t + \Delta t) = \dot{\varepsilon} \Delta t L_x(t)$ where Δt is the MD time integration step. The X-coordinate of all the atoms within the simulation cell is rescaled
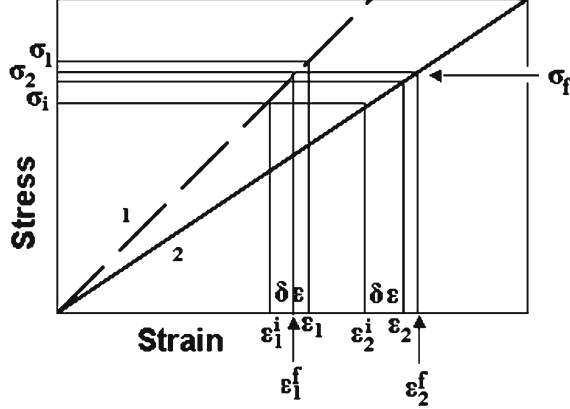
Figure 13. Illustration of the stress versus strain responses of the regions (1 and 2) of a mixed-potential inhomogeneous system. See text for details.

proportionately. From one MD integration time step to another, the mixed-potential glass is subjected to a uniform strain. That is, the two regions of the glass, 1 and 2 with different potential functions are strained by the same amount $\varepsilon = \varepsilon_1 = \varepsilon_2$. Application of this constant strain rate to the simulated glasses may lead to two different scenarios for the evolution of the mixed-potential system. If the strain rate is too fast, it may not allow the system to reach the condition for mechanical equilibrium, namely that the divergence of the stress tensor, $\mathrm{div}(\sigma)$ becomes zero. In that case the heterogeneous system will exhibit uniform strain and non-uniform stress profiles along the X-direction. On the other hand, if the strain rate of the mixed-potential system is slow enough to allow for thermodynamic equilibrium to be reached, then despite the fact that a uniform strain is applied at every MD time step, the system will relax toward the equilibrium state of uniform stress, namely $\sigma = \sigma_1 = \sigma_2$. This process is illustrated in Figure 13. We consider as a starting point the equilibrium state with initial stress, σ_i and strains ε_1^i and ε_2^i. We then apply a uniform strain $\delta\varepsilon$ that leads the regions 1 and 2 into a state with different stresses, $\sigma_1 \neq \sigma_2$. Relaxation toward a new state of mechanical equilibrium results in a uniform final stress, σ_f, and the strains ε_1^f and ε_2^f.

In that case, the state of strain of the two regions differs. The total strain must satisfy the condition: $\varepsilon = \varepsilon_1 r + \varepsilon_2 (1-r)$ where r is the ratio of the length of region 1 to the length of the entire system in their reference state for measuring strain. Failure will occur when the uniform stress becomes

$$\sigma^F = \min(\sigma_1^F, \sigma_2^F) \tag{8}$$

where σ_1^F and σ_2^F are the strengths of the two regions. The failure strain of the mixed potential system is then estimated by

$$\varepsilon^F = \min(\sigma_1^F, \sigma_2^F)/E_{\mathrm{eff}} \tag{9}$$

with the effective modulus of the inhomogeneous system given by

$$\frac{1}{E_{\mathrm{eff}}} = \left(\frac{r}{E_1} + \frac{1-r}{E_2} \right) \tag{10}$$

Here E_1 and E_2 are the Young's moduli of regions 1 and 2, respectively. Since the effective modulus of the mixed-potential system should take a value intermediate to that of the two reference systems, the failure strain of the mixed-potential system always will be lower than the failure strain of the CT and BKS reference glasses. From an atomistic point of view, the regions 1 and 2 are defined geometrically in terms of the width, W, without direct mention of the atomic content of these regions. Upon straining the mixed-potential glass, the fractional length of region 1 and 2 remains the same but the number of atoms within each region may vary. This relationship provides the mechanism for relaxation toward the state of uniform stress. After straining regions 1 and 2 uniformly, region 1 will be stressed differently from region 2. Atoms crossing the boundaries between the two regions enable a redistribution of strain and stress towards a uniform stress distribution throughout the simulation cell and a non-uniform strain, $\varepsilon_1 \neq \varepsilon_2$. It is worth noting that the orientation of the embedded region with respect to the direction of straining affects the behavior of the mixed-potential system considerably. Should the mixed-potential system be strained in a direction perpendicular to the X-direction (i.e. the two regions are strained in parallel now, while before they were strained in series), each region would be strained equally and the total stress would be given by:

$$\sigma = \sigma_1 r + \sigma_2 (1 - r) \tag{11}$$

The criterion for failure would then be given by (assuming that failure of one region would result in total failure):

$$\varepsilon^F = \min\left(\varepsilon_1^F, \varepsilon_2^F\right) \tag{12}$$

The failure stress would become:

$$\sigma^F = \varepsilon^F (E_1 r + E_2 (1 - r)) \tag{13}$$

We show, in Figure 14, the effect of the width of region 2, W, on the mechanical response of the mixed-potential glass to a constant strain rate of 0.005/ps. This strain rate is slow enough to allow the mixed-potential system to relax to a state of mechanical equilibrium. The responses of the CT and BKS reference systems also are displayed in Figure 14. In the elastic regime (small strain), the elastic modulus takes on as expected, values intermediate to those of the reference systems. The stress–strain curves approach those of the CT reference system as one decreases the width W of region 2, (i.e. as the contribution of the BKS potential decreases) in accordance with Eq. (10). The failure strain decreases with decreasing W in agreement with Eq. (9). Although the strength of the mixed system is significantly lower than that of the embedding system (CT reference), Eq. (8) is not satisfied. The strength of the mixed-potential system appears to increase with decreasing W, with a value very close to that of the BKS reference system for the widest region 2. This observation shows that the deviation does not result from a strain rate that is too fast but from the fact that as the BKS region narrows, the mechanism of failure by formation and coalescence of BKS-type voids cannot be accommodated. The mixed-potential system fails when the stress has reached a value sufficient for voids to form in region 1 and coalesce with those of the region 2. The size of the embedded-potential region is therefore of critical importance in mixed-potential multi-scale models. The embedded
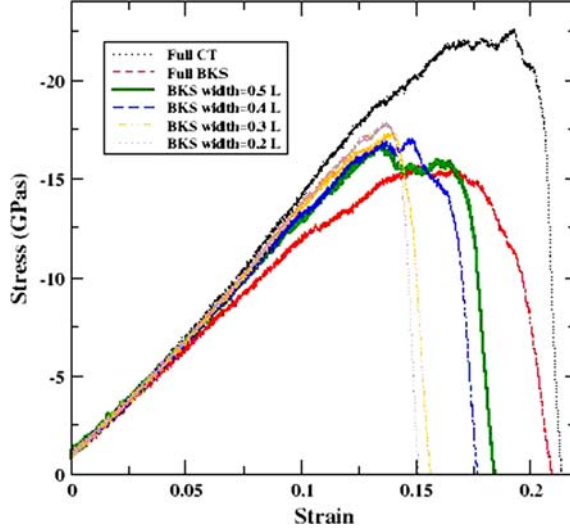
Figure 14. Stress versus strain curves for static mixed-potential systems with various widths of BKS potential region, W. The location P of the BKS region remains constant at $0.55L_x$. The strain rate = 0.005/ps and the initial glass configuration is that of sample 1.

region has to be large enough to include the proper mechanism for the physical phenomenon studied. In all the cases studied, failure occurs in the weaker region, that is, in region 2, independently of its width.

The effect of the location of the embedded region at fixed width is illustrated in Figure 15. We consider two mixed-potential systems simulated from the sample 1 initial configuration where the embedded region 2 is centered on the two locations: $0.6875L_x$ and $0.25L_x$. Figure 15 shows unambiguously that the response of the mixed-potential system is sensitive to the location of the BKS region, pointing to the inhomogeneous nature of the sample glass structure at the nano-scale. In these simulations, the width of the region 2 is $0.25L$. This width is sufficiently small for region 2 to be sensitive to the structural inhomogeneity of the initial glass configuration. In the two cases studied, the sample fractures at the location of the BKS region. This behavior makes apparent the bias on failure behavior that is imposed by a mixed-potential simulation with a predetermined position of the embedded potential region. The point is illustrated effectively in Figure 16 where, dividing the simulation cell into 64 slabs and using wavelet transforms, we track the location of the slab with the highest number of singly coordinated oxygen atoms. Initially and for both mixed systems, the slab located near $0.93L_x$ possesses the largest number of 1C-oxygen atoms. Application of the constant strain rate leads to the weakening of the glass in the BKS region forcing failure to occur at the location of the BKS region. In contrast to the mixed-potential systems the location of failure in the BKS reference system is at $0.55L_x$.

3.3. DYNAMICAL MIXED-POTENTIAL MULTI-SCALE SIMULATIONS

In this subsection we combine the findings of subsections (3.1) and (3.2) to investigate the dynamical behavior of mixed-potential systems. The dynamical mixed-potential
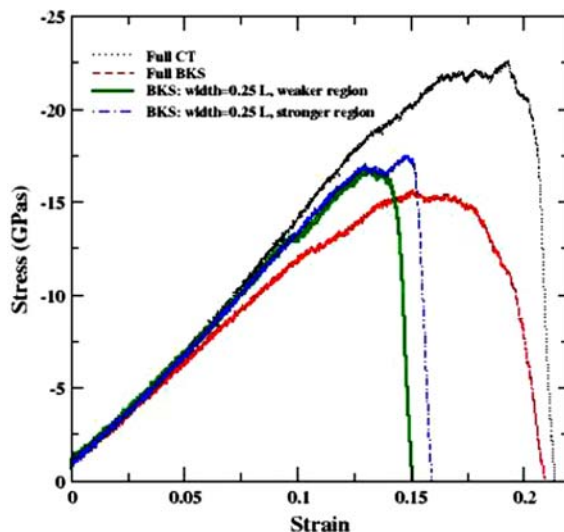
Figure 15. Effect of the location of the BKS region on the stress–strain curves of static mixed-potential systems. In both cases, the width of the BKS region is $0.25L_x$. The strain rate is 0.005/ps. The stress–strain curves of the reference CT and BKS systems are displayed also. The initial configuration is that of the glass sample 1.
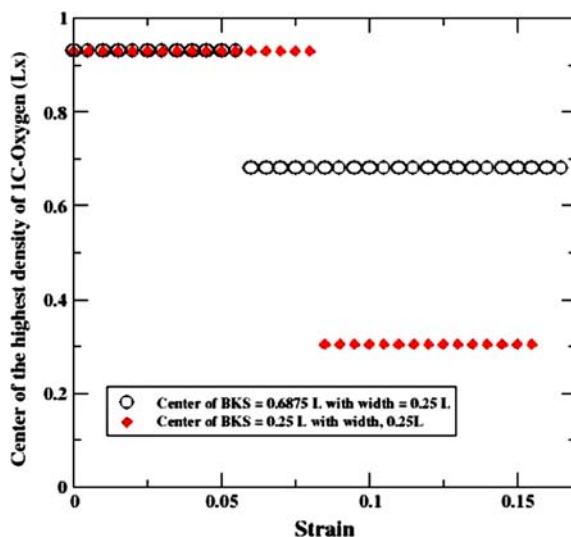

Figure 16. Evolution of the location of the slab with highest number of singly coordinated oxygen atoms per slab during the straining of the two static mixed-potentials systems of Figure 15. The center of highest number of singly coordinated oxygen atoms is determined with order 3 wavelet transforms.

system is composed of a BKS region of width $W = 0.5L_x$ embedded in a CT region. Wavelet approximations to the local density function, the singly coordinated oxygen function, and the local tensile stress per particle are used to identify, on-the-fly, the partitioning of the mixed system, i.e. the location, P, of the center of the BKS region. The wavelet approximations are all calculated up to second-order. The BKS region is centered on the slab with either the lowest value of the approximate density,
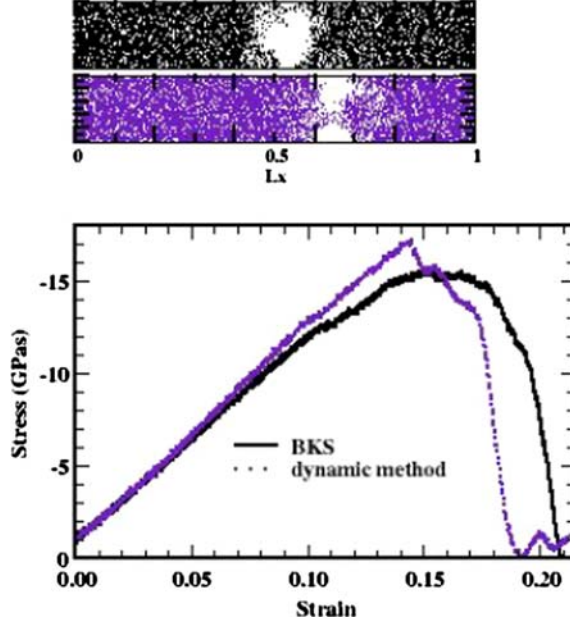
Figure 17. (a) Sample 1 after failure, top: reference BKS system and bottom: dynamical mixed potential system (lowest atomic density criterion for relocation of BKS region). $W = 0.5L_x$, $\Delta t_{update} = 100\ \Delta t$; (b) Stress–strain relationship for the reference system (BKS) and the dynamical mixed-potential system.

or the highest number of 1C oxygen atoms or the highest tensile stress per particle. The time between updates of the location of the BKS region, $\Delta t_{update,}$ emerges as an additional parameter in the dynamical simulation of mixed-potential multi-scale models. This time should not be so long as to lead to a nearly static mixed-potential simulation with its associated bias, nor should it be so short (lowest value is the MD integration time step, Δt) as to lead to large fluctuations in the location of the embedded region. In addition, to reduce large fluctuations in the location of region 2 associated with atomic vibrations, we calculate time averages of the local density, number of 1C oxygen atoms, and local stress/particle over 10 MD integration time steps prior to an update of the BKS region location.

We first evaluate the dynamical mixed-potential method with relocation of the BKS region on the slab with the lowest value of the second-order wavelet approximation to the local atomic density. Figure 17(a) shows that the dynamical mixed potential system does not fail at the same location as does the reference system. The calculated strength of the mixed-system exceeds that of the reference system. We have studied the effect of the update time, Δt_{update}, on the dynamical behavior of the mixed-potential model. In addition to $\Delta t_{update} = 100\ \Delta t$ (shown in Figure 17), we have considered update times of 50 and $200\ \Delta t$.

All the update times we studied result in glasses stronger than the reference BKS system (see Figure 18). The failure strain of the dynamic mixed-potential systems is lower than that of the reference system in accord with the observations made in the case of the static mixed-potential system. Furthermore, in all cases the glass sample does not fail at the correct location, $0.52L_x$ (see Figure 19). Rather, the failure location is 0.4, 0.63 and $0.8L_x$ for $\Delta t_{update} = 50$, 100 and 200 time steps, respectively.
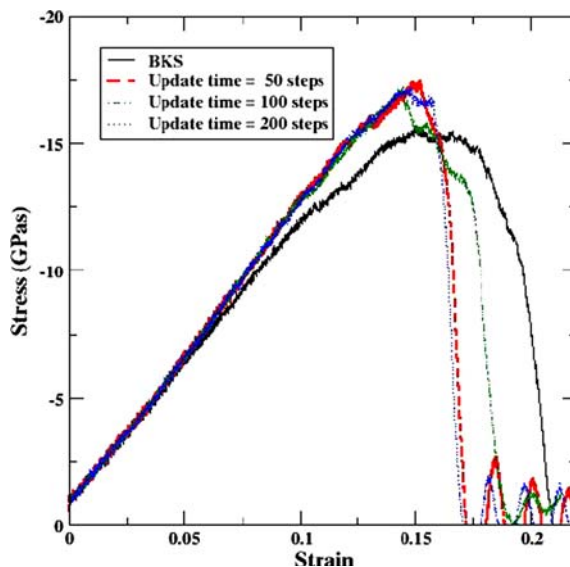
Figure 18. Stress–strain curves obtained with dynamical mixed-potential simulations. The update time is 50 (red), 100 (blue), and 200 (green) MD time steps. The stress–strain curve of the reference BKS system is in black.
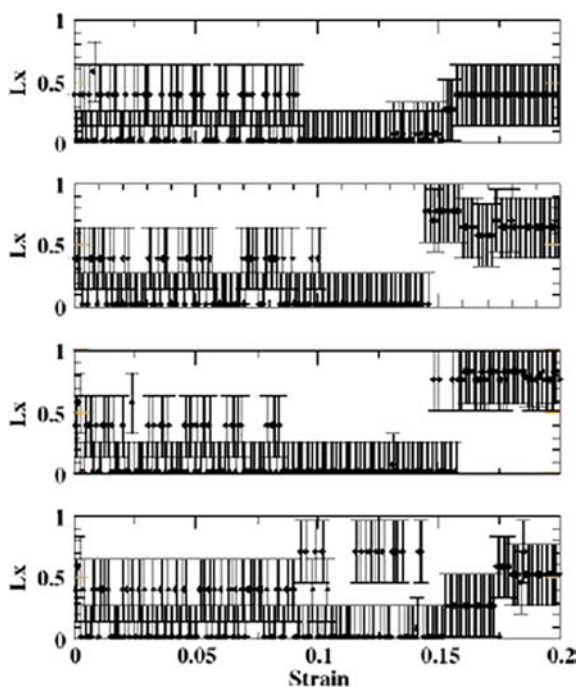

Figure 19. Location of the slab with lowest value of the wavelet-approximation of order 2 to the local atomic density function as a function of strain during dynamical simulations of mixed-potential model. The update time between relocation of the BKS region is 50, 100, and 200 time integration steps from the top panel down to the third one. The bottom panel is for the reference BKS system.

In Figure 19 it is interesting to note that the location of the embedded BKS region as a function of strain mimics that of the reference system in the elastic regime. It appears, however, that the lowest atomic-density criterion, when used for the relocation of the BKS region, traps that very region during the ductile part of the stress–strain curve (strain between 0.1 and 0.17). This behavior differs significantly from that of the reference system, which undergoes wild fluctuations in the ductile range of strains. This trapping resembles the static mixed-potential simulation and may lead to the deviation in location of failure as well as to the higher-than-normal strength of the sample. In the ductile range of the stress–strain curve, the region with lowest atomic density may not be the one that is the precursor to failure. The lowest density criterion does not appear to provide a robust, predictive means for dynamical partitioning of a mixed-potential system.

We turn therefore to the second possible criterion for relocation of the embedded BKS region, namely, the highest number of singly coordinated oxygen atoms. Here we consider the case of glass sample 1 with several update times: 200, 300, 500, and 800 MD steps. The stress–strain curve of the mixed-potential system exhibits again, as expected, a failure strain lower than that of the reference system (Figure 20). For all update times, the strength of this model exceeds that of the reference system significantly. In Figure 21, we observe that the location of the BKS region is reasonably stable over the elastic and ductile regions of the stress–strain curves. The latter region is very much narrowed. The width of the ductile region does not seem to be related to the choice of update time. Again it appears that, similar to what occurs with the density criterion, the BKS region remains trapped in a part of the glass sample that initially contained a comparatively large number of 1C oxygen atoms. Upon straining, the initial location of the BKS region in this defected part of the sample promotes a continuous increase in the number of defects in that region. That increase prevents the embedded region from sampling other parts of the glass. Relocation of the BKS region occurs after the very short ductile deformation of the glass. The time for relocation is therefore too sensitive to the heterogeneities of the initial structure of the glass and leads to a failure biased by those parts of the sample that are defective initially.

Figure 21 shows that the mixed-potential glass fails at 0.4, 0.8, 0.55, and $0.4L_x$ for the update times of 200, 300, 500, and 800 MD steps, respectively. Relocation every 500 MD steps gives the behavior closest to the reference system in terms of position of the final crack but fails to reproduce the strength of the glass sample.

Finally, we investigate the third criterion; It consists of using the wavelet approximations to the local tensile stress per particle to identify on-the-fly the location of the center of the embedded BKS region. We have tested various update times and found that with $\Delta t_{update} = 500\,\Delta t$, the dynamical mixed-potential models of samples 1 and 2 fail very similarly to the reference system (see Figures 22 and 23). Failure in the mixed systems occurs very near the location of failure of the reference BKS system. The strength of the mixed-potential models exceeds only slightly that of the reference system. The value of the failure strain exhibits some variability depending upon the number of neighboring slabs used to calculate the local stress. In most cases, the failure strain is lower than that of the reference system. However, in one case the failure strain exceeds that of the BKS system. In that case, the dynamical mixed-potential approach extends the ductile region of the glass.
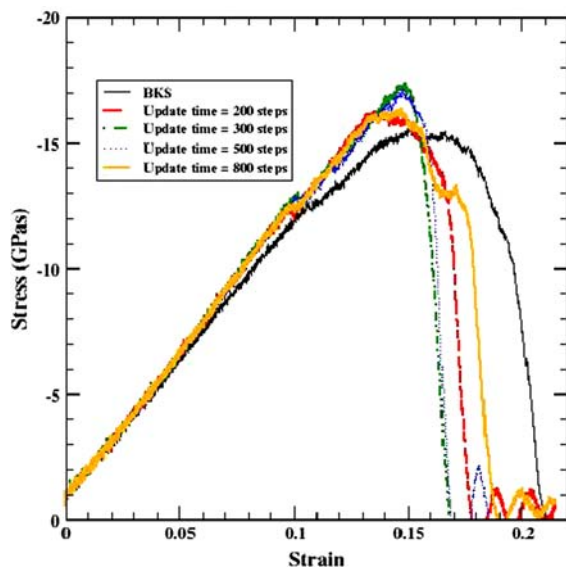
Figure 20. Stress–strain curves of the sample 1 reference system (BKS) and the dynamical mixed-potential system. Criterion for relocation of the embedded BKS region is the highest value of second-order wavelet approximation to the number of one-coordinated oxygen atoms. The updating times are 200 (red), 300(green), 500 (gray), and 800 Δt (yellow).
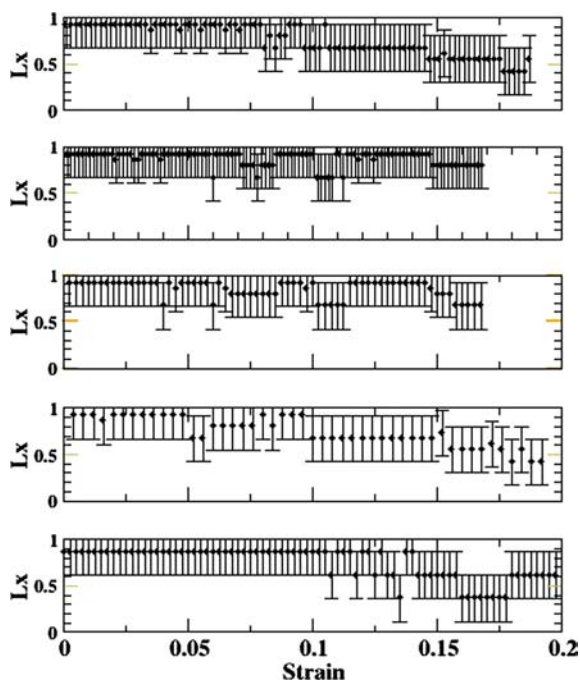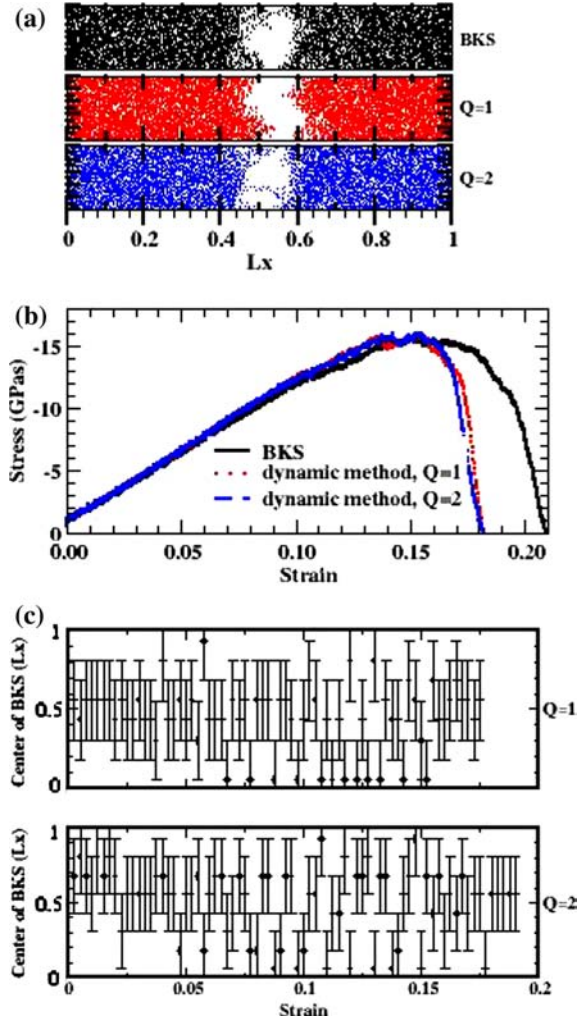

Figure 21. Location of the slab with highest value of the wavelet-approximation of order 2 to the local number of 1C oxygen atoms as a function of strain during dynamical simulations of mixed-potential model. The update time between relocation of the BKS region is 200, 300, 500 and 800 time integration steps from the top panel down to the fourth panel. The bottom panel is that of the reference BKS system.

Figure 22. Dynamical mixed-potential model of sample 1 subjected to a strain rate of 0.005/ps. The location of the embedded BKS region is identified as the slab with the highest value of the wavelet approximation to order 2 of the tensile stress per particle. The interval for updating the location of the BKS region is 500 MD time steps (or 0.5 ps). The local stress per particle is averaged over the last 10 MD steps (0.01 ps) prior to being used to relocate the embedded region. (a) Snapshots of the failed samples: top panel is the reference BKS system. Middle and bottom panels are the mixed systems with $Q=1$ and 2 respectively. (b) Stress–strain curves of the reference and mixed potential models. (c) Changes of BKS potential region in strain with $Q=1$ (upper) and $Q=2$ (lower).

This more ductile glass is the consequence of the swapping between the weaker BKS region 2 and the stronger CT region 2. The swapping leads to healing of defects (e.g. nano-voids) that may form in the BKS region between updating steps. In order to test that hypothesis, we have conducted a simulation of a mixed-potential system ($W=0.5L_x$) in which the swapping between regions 1 and 2 was performed at regular time intervals. During the inter-swap interval, we calculated and recorded the local stress as well as the number of atoms inside the two regions. A typical result of this simulation is plotted in Figure 24.
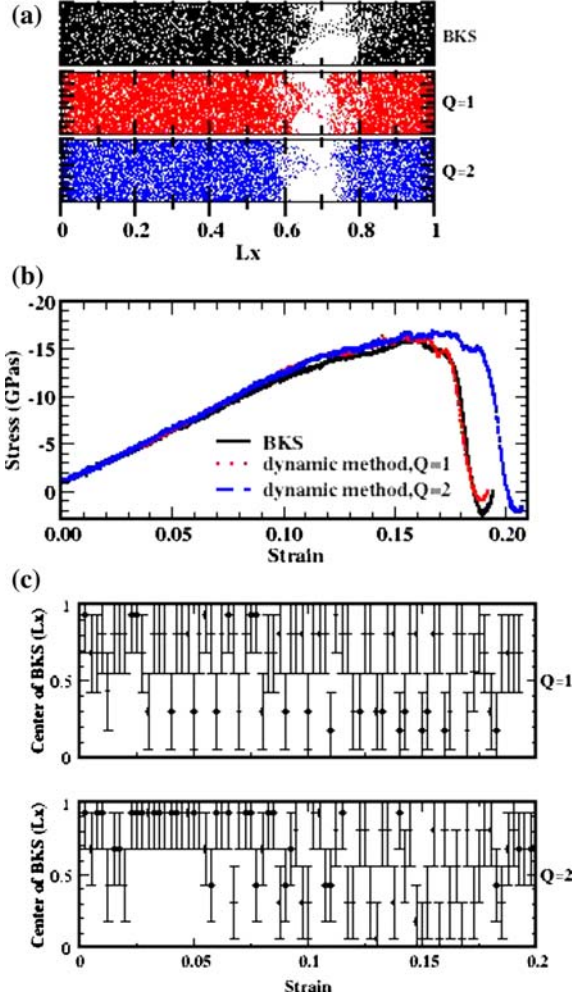
Figure 23. Same as Figure 22 but for glass sample 2.

The response of the mixed-potential system to relocation (swap) of the BKS and CT regions is easily visualized in Figure 25.

Consider an initial state with uniform stress throughout the heterogeneous system, σ_i. We assume that $r = 0.5$. The initial strain state of the two regions is $\varepsilon_1^i < \varepsilon_2^i$. This strain state is achieved by having fewer atoms in region 2 than in region 1. Upon swapping the regions (step A in Figure 24), i.e. interchanging the BKS and CT interactions, the new region 1 with a strain $\varepsilon_1^s = \varepsilon_2^i$ is now subjected to a stress, $\sigma_1 > \sigma_i$. The stress in the new region 2 with a strain $\varepsilon_2^s = \varepsilon_1^i$ is $\sigma_2 < \sigma_i$. These discontinuities in stress and strain are visible in Figure 24. After swapping the regions, the system evolves toward a state of mechanical equilibrium (uniform stress) with σ_2 increasing and σ_1 decreasing (step B) while simultaneously the strain in region 2 increases and the strain in region 1 decreases (process C). Since the regions always occupy $0.5L_x$ of the simulation cell along the X-axis, the change in strain is accompanied by a transfer of matter between the two regions as seen in Figure 24(a). At equilibrium, the number of atoms in region 2 should be less than the number of atoms in region 1.
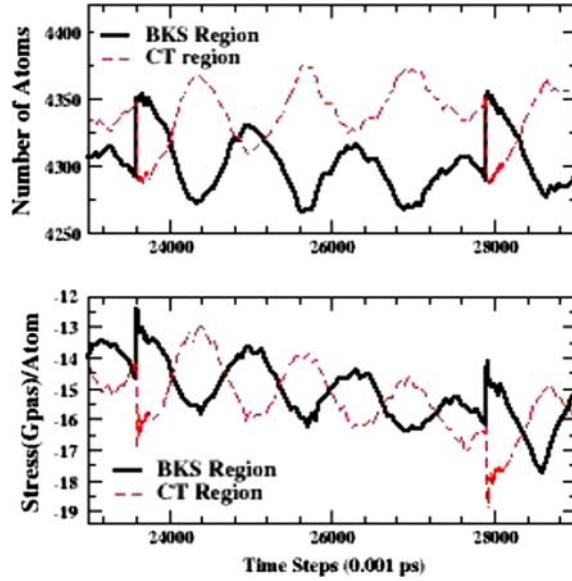
Figure 24. Time evolution (in units of MD time integration steps) of (a) number of atoms and (b) stress per particle in the embedded (BKS region) and embedding (CT region) partitions of the mixed-potential glass sample 1. The BKS and CT regions were swapped at time steps 23,600 and 28,000.
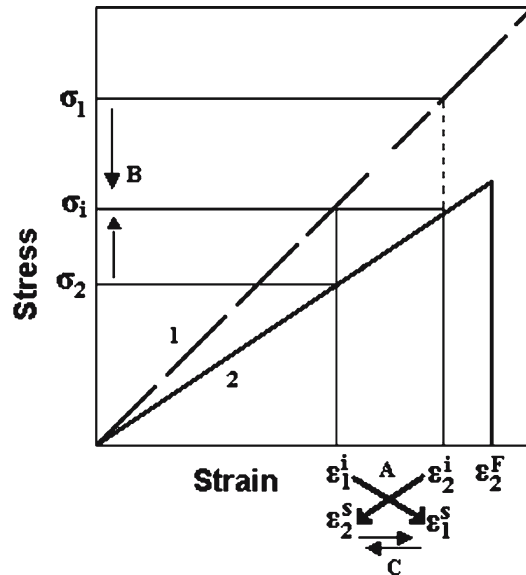

Figure 25. Illustration of the evolution of stress and strain during a swap of the embedded region (2) and the embedding region (1) in a dynamical mixed-potential simulation (see text for details).

This relaxation induces damped oscillations of the stress with a period that is associated with the nature of the regions. The entire process is purely an artifact of the relocation of the embedded region in a mixed-potential system that is equivalent to shocking the system. This shock should be present to some degree in any mixed-potential simulation with moving boundaries at which the inter-atomic force switch from one form to another.

Extending this relaxation behavior of a stress–strain curve of the embedded system with a non-linear regime, one can easily see that relaxation following swapping will lead to a densification (increase in density i.e. number of atoms) of the region undergoing ductile deformation prior to the swap. This process provides a mechanism for healing the weakest region (BKS region). Catastrophic failure will be retarded for a period of time longer than that of the reference system provided that the swap time is shorter than the time it takes for nano-voids to coalesce in the BKS region.

For instance, Figure 26 shows the failure behavior of glass sample 3 during two mixed-potential simulations with update time intervals, $\Delta t_{update} = 100 \, \Delta t$ (with a time for averaging the local stress of 10 Δt and $Q = 2$) and 800 Δt (averaging time 5 Δt and $Q = 1$). The wavelet approximations are of order 2. The mixed-potential method under these conditions allows the models to fail at the same location as that of the reference BKS simulation. However, the stress–strain curves show that the mixed models have extended ductile regions with strength exceeding that of the reference system. Comparison among samples 1, 2 and 3 suggests that the update time may not have a systematic impact on the stress–strain curves and, more specifically, the failure strain. The extension of the ductile region may be controlled by a complex and subtle combination of competing processes with different spatial and temporal scales of which the update time for relocation of the embedded region, the strain rate, the times for void formation and coalescence, the time for relaxation toward mechanical equilibrium, are all an integral part.

Glass sample 3 also was studied under the same update time conditions used for samples 1 and 2 ($\Delta t_{update} = 500 \, \Delta t$, with time averaging of 10 steps). These conditions were not able to reproduce the location of failure of the reference BKS state of sample 3, nor its strain–strain response, outcomes which indicate that the criterion for updating may be dependent on the size of the sample.

4. Conclusions

We have addressed several issues associated with the use of adaptive (on-the-fly) mixed-potential molecular dynamics simulation methods to simulate brittle fracture in amorphous glasses. Mixed-potential models are systems partitioned in different regions such that the inter-atomic forces are calculated using different inter-atomic potentials or methods (e.g. representing bonds with different level of complexity). Mixed-potential simulations have been used routinely to study systems subjected to heterogeneous stress distributions such as in the case of single crack propagation. For such models, one needs a high level of accuracy in the calculation of the inter-atomic forces in regions where large bond rearrangement or large bond stretching occur (e.g. near the tip of a crack), while a lower accuracy level is acceptable in the rest of the system (where bonds are subjected only to small deformations). The heterogeneity of the stress and strain field around a single crack renders the partitioning of the system easier. Here we have considered the failure of brittle amorphous silica subjected to a homogeneous strain with constant strain rate. We are concerned with establishing criteria for the identification, in real simulation time, of the most probable region of failure of the glass and its application to implementing an on-the-fly method for partitioning the system. Our mixed-potential system consists of a simulation cell partitioned into two regions with two different classical inter-atomic potentials.
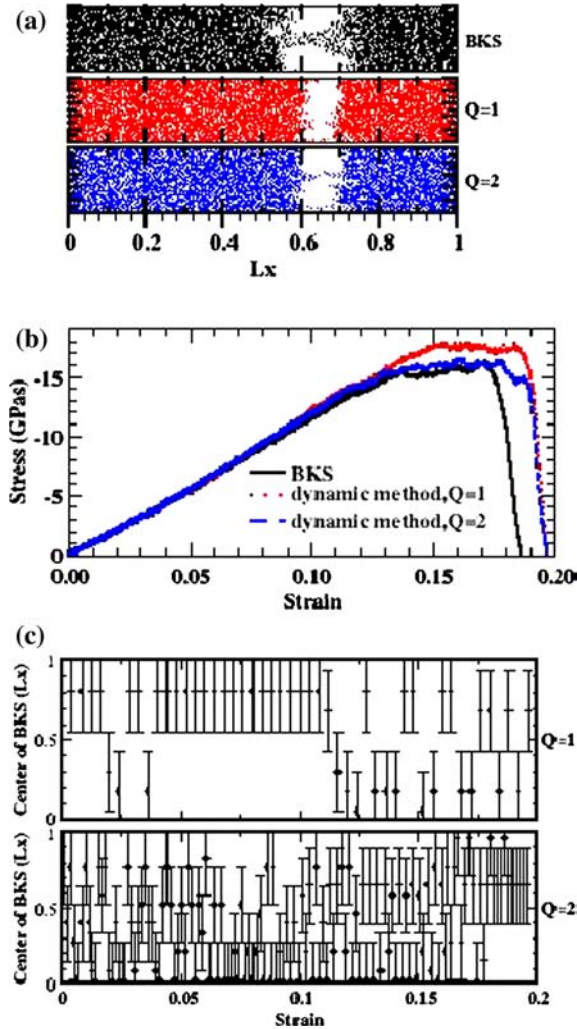
Figure 26. Dynamical mixed-potential model of sample 3 subjected to a strain rate of 0.005/ps. The location of the embedded BKS region is identified as the slab with the highest value of the order-2 wavelet approximation to the tensile stress per particle. The interval for updating the location of the BKS region is 100 MD time steps (red) and 800 steps (blue). (a) Snapshots of the failed samples: top image is the reference BKS system. Middle and bottom images are the mixed systems with $Q = 2$ and 1, respectively. (b) Stress–strain curves of the reference and mixed potential models. (c) Change of the BKS potential region in strain with $Q = 1$ (upper) and $Q = 2$ (lower).

Several criteria and constraints (some of which may seem obvious) must be satisfied for conducting mixed-potential simulations:

(a) The inter-atomic potentials should yield glasses with same elastic properties.
(b) The strength of the glass simulated with the embedding potential should exceed that of the embedded potential, otherwise failure will occur in the embedding region.
(c) The geometry of the embedded/embedding system should be consistent with the way the model is loaded or strained. Mixed-potential systems are composite systems and the laws that govern their failure depend on geometry and direction.

For instance, uniaxial straining applied to a mixed system with boundaries parallel or perpendicular to the axis of straining will not yield the same strength of the composite.

(d) The dimension and location of the embedded region plays a major role in determining the nature of failure. The embedded region has to be large enough to account fully for the mechanism of failure of the glass. Silica glasses under uniform strain fail by formation and coalescence of voids. The embedded region cannot be so small as to exclude or inhibit these two phenomena. Glass structures are intrinsically heterogeneous with spatial variations in density and/or defect content. Failure will occur within the weaker embedded region irrespective of the initial glass structure.

(e) The behavior of mixed-potential systems with a dynamically moving embedded region depends strongly upon the criterion used to relocate that region. This failure behavior appears to be controlled by a complex, subtle combination of competing processes with different spatial and temporal scales of which the update time for relocation of the embedded region, the strain rate, the times for void formation and coalescence, and the time for relaxation toward mechanical equilibrium play an important role.

(f) Wavelet approximations to spatially varying functions such as the local atomic density, number of singly coordinated oxygen atoms, and the local stress per particle have the ability to filter out unwanted fluctuations in the time evolution of the center of the embedded region.

(g) Among the criteria for relocation of the embedded region, wavelet approximations to the local stress per particle along uniaxially strained glasses enable mixed-potential simulations to reproduce the strength and location of failure of the single potential reference glass.

(h) The choice of time for updating the location of the embedded region, and the order of the wavelet approximation to the local stress per particle may depend on the geometry and size of the glass studied.

Acknowledgement

References

1. Wiederhorn, S.M., J. Am. Ceram. Soc. 50 (1967) 407.
2. Wiederhorn, S.M., and Bolz, L.H., J. Am. Ceram. Soc. 53 (1970) 543.
3. Proctor, B.A., Phys. Chem. Glasses 31 (1990) 78.
4. van Beest, B.W.H., Kramer, G.J., and van Santeen, R.A., Phys. Rev. Lett. 64 (1990) 1955; the modification to the BKS potential was suggested by L.R. Corrales, private communication.
5. Alavi, A., Alvarez, L.J., Elliot, S.R., and McDonald, I.R., Philos. Mag. B 65 (1992) 489.
6. Hoover, W.G., Phys. Rev. A 31 (1985) 1695; Nosé, S. Mol. Phys. 52 (1984) 255.
7. Beeman, D., J. Comput. Phys. 20 (1976) 130.
8. Ewald, P., Ann. Phys. 64 (1921) 253.
9. Huff, N.T., Demiralp, E., Cagin, T., and Goddard III, W.A., J. Non-Cryst. Solids 253 (1999) 133.

10. Askar, A., Cetin, A.E. and Rabitz, H., J. Phys. Chem. 100 (1996) 19165.
11. I. Daubechies, Ten Lectures on Wavelets, Regional Conference Series In Applied Mathematics, Vol. 61, SIAM, Philadelphia PA, 1992.
12. Abbate, A., Das, P. and Decusatis, C.M., Wavelets and Subbands: Fundamentals and Applications, Birkhäuser, Boston, 2002.
13. Frantziskonis, G. and Deymier, P.A., Model. Simul. Mater. Sci. Eng. 8 (2000) 649.
14. Frantziskonis, G. and Deymier, P., Phys. Rev. B 68 (2003) 024105.